

Zero Field Assembly of Long Magnetic Dipolar Chains in 2D Polymer Nanocomposite Films

Christian Appel,^{*,†} Björn Kuttich,[†] Lukas Stühn,[‡] Robert W. Stark,[‡] and Bernd Stühn[†]

[†]*Institute of Condensed Matter Physics, Technische Universität Darmstadt,
Hochschulstr. 8, D-64289 Darmstadt, Germany*

[‡]*Physics of Surfaces, Technische Universität Darmstadt, Alarich-Weiss-Str. 16,
D-64287 Darmstadt, Germany*

E-mail: christian.appel@fkp.physik.tu-darmstadt.de

Abstract

The existence of magnetic dipolar nanoparticle chains at zero field has been predicted theoretically for decades, but these structures are rarely observed experimentally. A prerequisite is a permanent magnetic moment on the particles forming the chain. Here we report on the observation of magnetic dipolar chains of spherical iron oxide nanoparticles with a diameter of 12.8 nm. The nanoparticles are embedded in an ultrathin polymer film. Due to the high viscosity of the polymer matrix, the dominating aggregation mechanism is driven by dipolar interactions. Smaller iron oxide nanoparticles (9.4 nm) show no permanent magnetic moment and do not form chains but compact aggregates. Mixed monolayers of different iron oxide nanoparticles and polymer at the air-water interface are characterized by Langmuir isotherms and in-situ X-ray reflectometry (XRR). The combination of the particles with a polymer leads to a stable polymer nanocomposite film at the air-water interface. XRR ex-

periments show that nanoparticles are immersed in a thin polymer matrix of 3 nm. Using atomic force microscopy (AFM) on Langmuir-Blodgett films, we measure the lateral distribution of particles in the film. An analysis of single structures within transferred films results in fractal dimensions that are in excellent agreement with 2D simulations.

Introduction

Due to their perfect combination of well adjustable macroscopic properties, polymer nanocomposites have attracted a lot of research interest in recent years. The polymeric component of the composites serves as a matrix in which a wide range of nanoparticles can be introduced in order to achieve desired thermal, rheological, optical, conductive, magnetic, etc. properties.¹⁻⁵ While tuning of these properties is of outstanding interest in most applied research, fundamental studies focused on the precise interactions between polymer and particles as well as on the microstructure of the nanoparticles distributed in the polymer matrix.⁶⁻⁹ To prevent nanoparticles from aggregation they are stabilised by a shell.¹⁰ The use of carboxyl acids, such as oleic acid, as shell ligands leads to a steric stabilisation of the particles. In a composite the shell type strongly influences the interaction between nanoparticles and polymer matrix.

Metal nanoparticles are not only characterized by their high surface to volume ratio but also by quantum confinement.¹¹ Most prominent among these are gold nanoparticles, especially in combination with polymers, because of their localised surface plasmon resonance, allowing for many sensor applications.^{1,12,13} Besides these, nanoparticles composed of iron, nickel and cobalt have come more and more into focus because of their outstanding magnetic properties.¹⁴⁻¹⁶ Sufficiently small particles (size ≈ 100 nm) consist only of one single ferromagnetic domain, while for even smaller particles the permanent magnetisation completely vanishes. The material is below its Curie temperature but its magnetic dipole moment flips on a fast timescale. This state is known as superparamagnetic.^{14,17,18} Introducing magnetic

particles into a non-magnetic solvent yields a so-called ferrofluid, which offers the possibility to investigate fundamental magnetic dipole-dipole interactions.¹⁹⁻²² A polymer nanocomposite consisting of magnetic nanoparticles can be understood as a ferrofluid-like system with a highly viscous solvent. Due to the high viscosity, Brownian dynamics are significantly slowed down. It may therefore be expected that aggregation of nanoparticles is unlikely to be limited by diffusion (DLA) but dominated by magnetic interactions. This effect is particularly interesting when the system's degrees of freedom are reduced to two dimensions (2D). Firstly, the probability of direct particle interaction is increased due to the 2D confinement. Secondly, aggregated structures can be visualized directly by real space methods. At the air-water interface, polymer and nanoparticles can be prepared into an ultra thin film and investigated by various experimental methods.

In the following we will investigate the influence of particle size on the dipolar interactions and the impact on structure formation of nanoparticles inside a polymer monolayer. We choose to study spherical iron oxide nanoparticles having sizes between 5 nm and 20 nm which are commercially available and should be close to the limiting size for expected superparamagnetic behaviour.²³⁻²⁵ They are stabilised by a hydrophobic oleic acid shell. The used polymer is a hydrophilic-hydrophobic diblock copolymer. For the preparation of the nanocomposite film we make use of the air-water interface and the fact that both nanoparticles and the used polymer are surface active and thus form stable monolayers at this interface.

The properties of the polymer at the air-water interface have been investigated recently.²⁶ It forms a thin layer with thickness between 2 nm and 3 nm. In the present study we first characterise three iron oxide nanoparticles of different sizes by small angle X-ray scattering. We investigate their capability to form stable monolayers at the air-water interface using Langmuir isotherms and in-situ X-ray reflectivity (XRR). Our main interest lies in the properties of the combined films of nanoparticles and polymer. First, the aforementioned experimental techniques are used to determine the properties of the composite films. We then

turn to the question of the structure of nanoparticle aggregates forming within the polymer layer. Depending on the aggregation mechanism being diffusion limited (DLA) or dominated by magnetic dipole interaction, the appearance of differently formed clusters is predicted.^{27,28} We use atomic force microscopy (AFM) on ex-situ samples (Langmuir-Blodgett (LB) films) to answer this question.

Experimental Section

Samples

Samples used in this work are three different sizes of iron oxide nanoparticles (diameter: 5, 10 and 20 nm) and a diblock copolymer poly(ethylene glycol)-*b*-poly(*n*-butyl acrylate) (PEG₆-*b*-P*n*BA₁₃₂, M_n = 17.2 kg/mol). The polymer was synthesized via controlled living polymerization as described in our previous publication.²⁶ The iron oxide nanoparticles were purchased from *Ocean Nanotech* where their size and shape was characterized by TEM experiments. The 5 nm particles (FeNP5) are stated to consist of a mixture of Fe₂O₃ and Fe₃O₄, while the 10 nm (FeNP10) and 20 nm (FeNP20) ones are claimed to only consist of Fe₃O₄ nanocrystals. Particles were purchased dissolved in chloroform and stabilized by an oleic acid shell of 2.5 nm thickness according to the supplier.

Pressure-Area Isotherms

Pressure-area isotherms were performed on a KSV NIMA trough system (KSV NIMA, Langmuir Troughs KN 1006, Biolin Scientific) equipped with two hydrophobic symmetrically-moving barriers and a Wilhelmy platinum plate placed exactly in-between those barriers (45°- tilted with respect to the direction of compression) at room temperature of 22 ± 1 °C. The trough dimensions are (58 x 14.5) cm². For each measurement both barriers and the trough are first cleaned with ethanol and rinsed with purified water. We use deionized Millipore water (Millipore Direct-Q) with a specific resistivity of 18.2 MΩ cm at 25 °C for

rinsing and for the subphase. All isotherms were measured on a water surface and the purity of the surface was checked prior to each measurement by a compression of the water surface with $2175 \text{ mm}^2/\text{min}$ while the surface pressure was monitored ($\Delta\Pi < 0.3 \text{ mN/m}$). The iron oxide nanoparticles and composite samples were dissolved in chloroform (concentration $c \approx 5.0 \text{ mg/ml}$) and mixed before each measurement (Vortex 2000 mixer). For the composite samples the concentrations were $c_{\text{PnBA}} = 1 \text{ mg/ml}$: $c_{\text{FeNP}} = 1\text{...}3 \text{ mg/ml}$ so that area fractions of nanoparticles spread at the interface are comparable for both systems (3 % particle coverage at maximum trough area). A specified volume V was spread in drops of $1.5 \mu\text{l}$ on the water subphase with a Hamilton syringe (maximum volume $5 \mu\text{l}$). The chloroform evaporated quickly and the composite formed stable monolayers. All isotherms were measured after a waiting time of 30 min. The available surface for each object (i.e. nanoparticle or polymer molecule) is given by the mean molecular area mmA , which is defined as:

$$\text{mmA} = \frac{AM}{cVN_A} \quad (1)$$

A is the actual area enclosed by the two barriers, M the molecular weight of the object and N_A the Avogadro constant. In case of the polymer nanocomposites, mmA was calculated for the polymer chain solely in order to compare to the pure polymer isotherm. We subtracted the area occupied by nanoparticles from the area enclosed by the two barriers (A) to get the correct mmA for a polymer chain.

The second parameter is the surface pressure Π given by

$$\Pi = \gamma_0 - \gamma \quad (2)$$

where γ_0 is the surface tension of the subphase (water) and γ the surface tension of the system after spreading the sample. The layers were compressed with a constant velocity of $435 \text{ mm}^2 \text{ min}^{-1}$. Isotherms were repeated at least three times to check for the reproducibility of the results.

X-ray Reflectometry

Experiments were performed on a modified D8 Advance reflectometer (Bruker AXS, Germany). The design of the setup enables us to measure reflectivities in $\theta - \theta$ geometry with the X-ray source and detector attached at goniometer arms which can be moved independently with a precision of 0.001° . A conventional X-ray tube with a Cu anode (CuK_α , wavelength $\lambda = 1.54 \text{ \AA}$) is used to generate a X-ray beam with a line focus. The beam is further monochromized by a Goebel mirror (W/Si multilayer mirror). Through a narrow horizontal slit of 0.1 mm, the beam passes an absorber (calibrated Cu attenuator) which is necessary for high intensities near the critical angle in order to maintain a linear response of the detector. A second 0.1 mm horizontal slit is placed after the absorber to cut out the K_β -line (which is also reflected by the monochromator). Soller slits ($\Delta\theta_x = 25 \text{ mrad}$) are placed after the last horizontal slit and directly in front of the detector.

Intensity is detected by a Vantec-1 line detector (Bruker AXS, Germany) providing the possibility to measure the specularly reflected intensity and the diffuse intensity simultaneously in an angular range of $\Delta\theta_f = 2^\circ$ for a given incident angle θ_i . For each incident angle θ_i , a single intensity $I(\theta_f)$ contains the specular and off-specular scattering. The intensity of the reflected beam is determined as the integral over the specular peak corrected for background measured as the diffuse intensity. The specular reflectivities were analyzed using the Motofit Reflectometry package, rev. 409²⁹ for IGOR Pro.

Langmuir-Blodgett Films

LB films were produced on a Langmuir trough system (μ Trough System Kibron Inc., Helsinki Finland). The silicon wafers were cleaned for 2 minutes in piranha solution and their surface was characterized by XRR measurements prior to the transfer of the monolayers. For the transfer, the silicon wafers were first dipped through the monolayer in the subphase with a dipping speed of 2 mm/min, and then pulled out of the subphase through the monolayer again at the same speed. The molecular area of the film was controlled and monitored by

a software to guarantee a constant pressure during the transfer. The data shows that the monolayer was transferred when the silicon wafer was pulled out of the subphase (Z-type LB film) and all transfer ratios were 80 – 100 %.

Small Angle X-ray Scattering

SAXS was performed using a laboratory X-ray set-up. The K_{α} -line of a conventional copper X-ray tube with a wave length of $\lambda = 1.54 \text{ \AA}$ is used and further monochromated by a X-ray mirror. The point focused beam is collimated by three pinholes. The detector-sample distance is 1.5 m and calibration of the scattering vector q is done by measuring the first peak of silver behenate as a calibration sample.³⁰ The scattering vector is defined as $|\vec{q}| = 4\pi/\lambda \sin \theta$, with 2θ being the scattering angle. The scattered intensities are measured with a two-dimensional multi-wire gas detector (Molecular Metrology, 1024×1024 pixels). The overall instrumental resolution is estimated to be $\Delta q = 0.01 \text{ \AA}^{-1}$ by the full width half maximum of the silver behenate peak during calibration. The accessible q range is $0.007 \text{ \AA}^{-1} \leq q \leq 0.25 \text{ \AA}^{-1}$ and the data was radially averaged because all scattering was isotropic.

Atomic Force Microscopy

AFM images of polymer nanocomposite LB films were measured with a Cypher S AFM (Asylum Research Oxford Instruments) in amplitude modulation mode. Cantilevers (BudgetSensors and Olympus) with spring constants between 2 N/m and 3 N/m, resonance frequencies between 70 kHz and 75 kHz and tip radii smaller than 10 nm were used. As feedback signal, the ratio of setpoint and free amplitude was kept at 0.6 with a free amplitude of about 30 nm. Scan rates varied between 0.2 and 2 lines per second, depending on the scan size. Measurements were performed in air under ambient conditions. To correct for scanner drift, height images were second order flattened using the free software Gwyddion.³¹ For further analysis, nanoparticles were identified via a height threshold of 4 nm.

Properties of Iron Oxide Nanoparticles

Size and Shape of the Nanoparticles

Small angle X-ray scattering was performed on nanoparticle bulk solutions. The solvent was changed to toluene in order to avoid the strong X-ray absorbance of chloroform and diluted to low concentrations ($c = 1 \text{ mg/ml}$). Resulting scattering profiles are shown in figure 1. In all cases, the scattering at small q displays a plateau indicating single particle scattering. The scattering from FeNP5 is fundamentally different compared to the other two sizes. For FeNP10 and FeNP20, clear oscillations are visible and intensity decays much faster ($I \sim q^{-4}$) compared to the small ones ($I \sim q^{-2}$). The scattering from the large particles can be described by a spherical form factor with a polydisperse radius (polydispersity: PDI, details see ESI). This is not possible for FeNP5, due to the weaker decaying intensity. Scattering from the smallest particles is modelled by an oblate spheroid form factor averaged over all possible orientations. Thus, the described objects are anisotropic with a major and minor diameter. For these particles it is possible to determine a radius polydispersity due to the orientation average. The oleic acid shell is not considered in the fitting, due to the missing contrast between oleic acid and toluene. Details on both form factors are given in the electronic supplementary information (ESI).

For all particle sizes a very good agreement between model and experimental data is found as demonstrated by the full black lines in the figure. The important parameters for data fitting are summarized in the table above figure 1. The results agree with the claimed sizes provided by *Ocean Nanotech*. However, the shape of FeNP5 particles is not spherical which leads to an additional degree of freedom for their orientation at the air-water interface. Since all small angle scattering data could be described by form factors only, the nanoparticles have to be dispersed homogeneously in the solvent. Thus, changing the solvent from chloroform to toluene did not lead to aggregation of the particles.

sample name	fit type	diameter _{major}	diameter _{minor}	PDI
FeNP ₅	spheroid	9.4 ± 0.1 nm	3.7 ± 0.1 nm	-
FeNP ₁₀	sphere	12.8 ± 0.1 nm	12.8 ± 0.1 nm	0.10 ± 0.03
FeNP ₂₀	sphere	21.4 ± 0.1 nm	21.4 ± 0.1 nm	0.11 ± 0.02

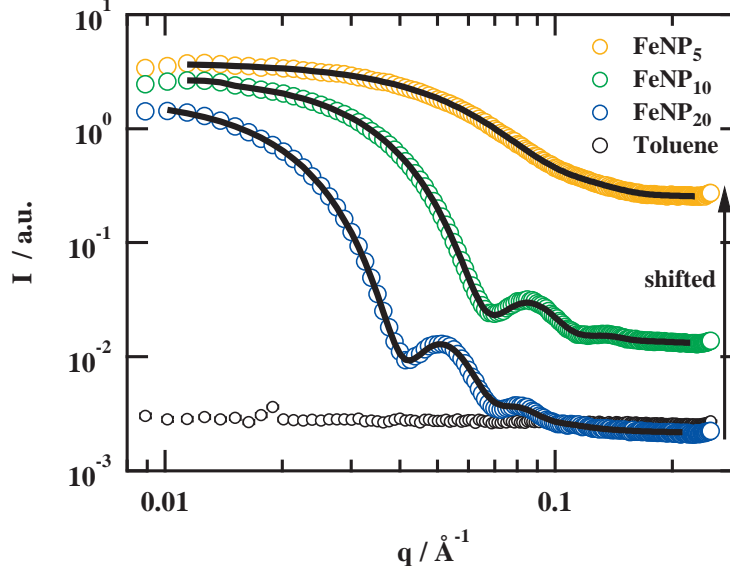


Figure 1: Small angle scattering data from the three different iron oxide nanoparticle sizes (FeNP5, FeNP10 and FeNP20). Very good agreement between fits and raw data is demonstrated using a polydisperse form factor of a sphere (FeNP10 and FeNP20) and a spheroid (FeNP5). The fit parameters for the models are summarized in the table above the figure.

Iron Oxide Nanoparticles at the Air-Water Interface

Langmuir monolayers were prepared for all three particles sizes at low surface coverage. Compression isotherms and *in-situ* specular reflectivities were measured for the particle films. Furthermore, the elastic modulus

$$E = -\text{mmA} \left(\frac{\partial \Pi}{\partial \text{mmA}} \right) \quad (3)$$

was calculated from the isotherms as a measure for the resistance of the film upon compression. No stable film is formed for FeNP20 particles. Compression isotherms and specular reflectivities shown in the supporting information strongly indicate that FeNP20 particles aggregate after being spread on the air-water interface. Surface pressure is already signif-

icantly increased for mean molecular areas thirty times larger than the projected particle area measured by SAXS. XRR shows only a rough surface. A similar behaviour is observed in a previous study.³² However, FeNP5 and FeNP10 form stable single layer particle films at the air-water interface. In the following we will focus on the properties of these nanoparticles and their polymer composites.

Langmuir Isotherms of Nanoparticle Layers

We start with the compression behaviour of single particle films of FeNP5 and FeNP10 prepared at the air-water interface. The isotherm and elastic modulus of FeNP5 films is shown in the left panel of figure 2. For low surface coverage, the surface pressure remained low ($\Pi < 1 \text{ mN/m}$) not affected by compression of the film. The film can be easily compressed ($E \approx 2 \text{ mN/m}$) indicating that mmA is much larger than the actual size of the particles. Upon decreasing the area to $\text{mmA} = 110 \text{ nm}^2$, the surface pressure increases with a linear slope. The resistance of the film upon compression increases indicated by the higher modulus E ($15 - 23 \text{ mN/m}$). Further compression leads to a shoulder in the isotherm at $\text{mmA} \approx 40 \text{ nm}^2$ accompanied by a sharp maximum in E .

The particle film is resisting further compression before structural changes in the film lead to a release of the stress. The two dashed black lines in the left panel of figure 2 denote the minimum and maximum projected area of the spheroidal particles based on their size as determined by SAXS. Here we take an oleic shell thickness of 1.25 nm into account, thus allowing for interpenetration of shells. Even for this densely packed configuration the minimum projected area is significantly larger than the position of the observed shoulder in the isotherm. This points to an inappropriate determination of the mmA . A possible reason is an incorrect value of the amount of particles spread on the surface. We will discuss this in detail later on when looking at the XRR profiles.

The observed shoulder in the isotherm may be explained by either a collective flipping of the ellipsoidal particles, or by buckling of the film and multilayer formation. A collective

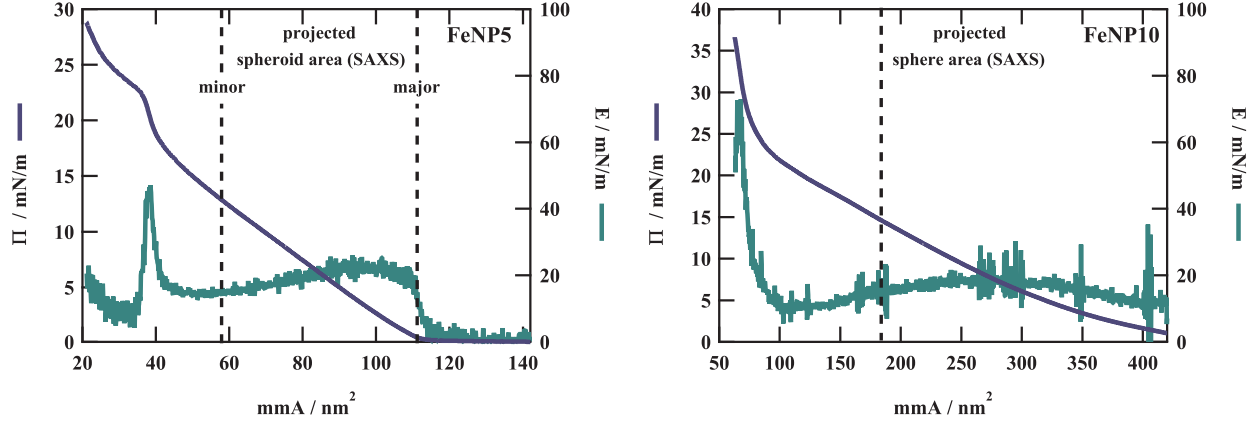


Figure 2: Langmuir isotherms presented as surface pressure (Π) vs. mean molecular area (mmA) for FeNP5 and FeNP10. The elastic modulus (E) computed from the isotherms is depicted as well (right axis). The vertical dashed lines represent the projected area for fully interpenetrating shells derived from the SAXS sizes (details see text).

flipping process seems to be very unlikely, instead single flips due to a locally increased density in the monolayer are expected.³³ Thus, we suppose that buckling of the film is responsible for the observed feature in the isotherm, which will be further investigated by in-situ X-ray reflectivity and discussed in the following paragraph.

The right panel of figure 2 shows the isotherm and elastic modulus of FeNP10 films. The films were also prepared for low surface coverage ($\Pi \approx 1$ mN/m), however the pressure immediately started to increase with compression of the film. From $\text{mmA} = 300 \text{ nm}^2$ to 100 nm^2 , the surface pressure increases with a linear slope. In this region the resistance of the film, characterised by the elastic modulus (E ranging between $12 - 20$ mN/m), is similar to the smaller particles at the same surface pressure. Afterwards, the slope of the isotherm starts to change and increases more strongly. As already seen for the FeNP5 system, the projected particle area deduced from SAXS results is much larger than this feature of the isotherm. This discrepancy will be further discussed in the following section. In contrast to the FeNP5 film no shoulder in the isotherm is observed.

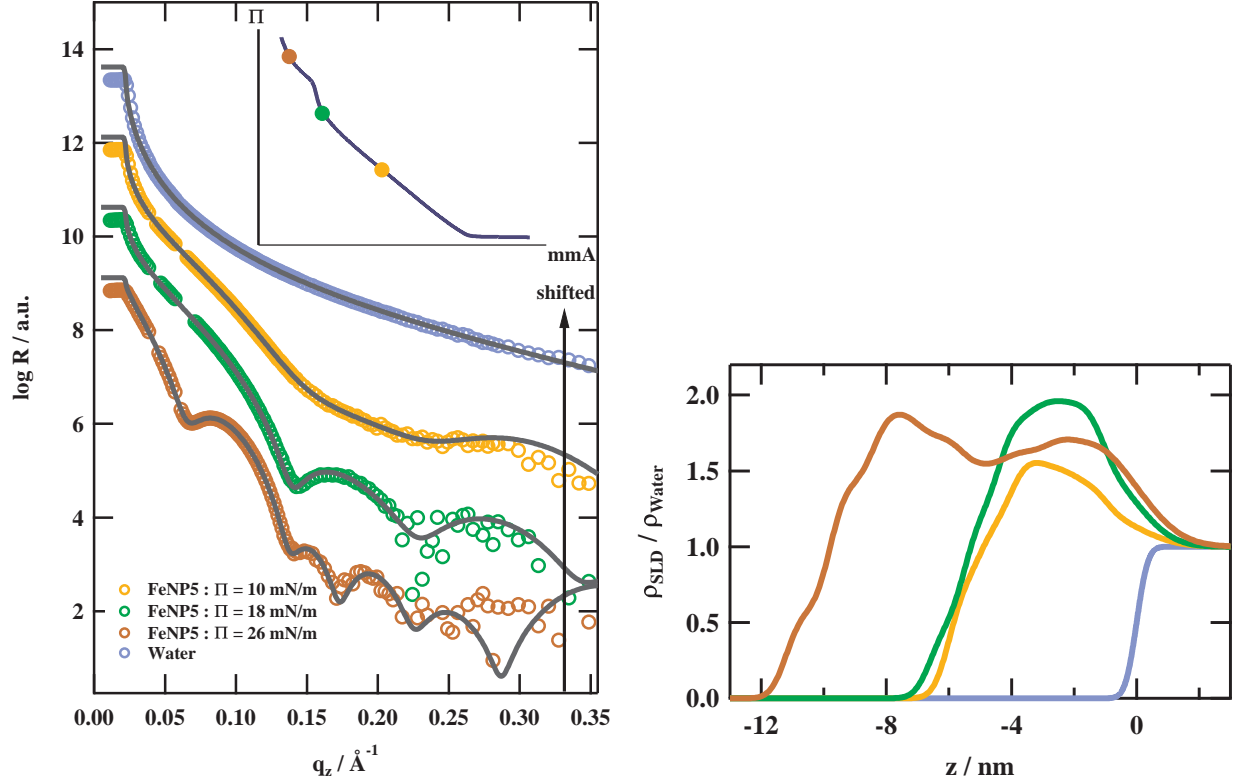
The change in the slope of the isotherm is accompanied by an increase of E up to 75 mN/m . The magnitude of the modulus helps to identify the structural state of the two particle films. Elastic moduli for nanoparticle films have been observed to range between

10 mN/m and up to several 100 mN/m.^{34,35} The maximum modulus depends on shell ligand, size distribution and spacing between the particles. Our samples have a maximum of $E \approx 48$ mN/m for FeNP5 and $E \approx 75$ mN/m for FeNP10 which is in agreement with published data on iron oxide nanoparticles.³⁶ Both values agree with the modulus characteristic for an oleic acid monolayer in the liquid-expanded state.³⁷ In case of the FeNP5 films, the value is considerably lower because the isotherm indicates that structural changes occur in the film before the modulus increases further. The sharp increase can be understood as resistance of the oleic acid ligand because further interdigitation of the ligand is restricted by its double bond that reduces their ability to interpenetrate. We interpret the lower value of $E \approx 12 - 23$ mN/m in the first part of both isotherms as a resistance of rather loosely connected groups of particles that slide past each other while the maximum represents real compression of the shell in a dense layer.

Vertical Density Profiles of Nanoparticle Layers at the Air-Water Interface

Film thickness was determined by specular reflectivity measurements for several positions in the isotherm of both particle sizes. Due to the high scattering contrast of the particles, an interference pattern can be clearly identified in the raw data (see figures 3 and 5) compared to the reflectivity of the bare water interface. When surface pressure is increased, the number of minima in the reflectivity increases. They become more distinct and shift to smaller q at high surface pressure. These patterns confirm the formation of a particle film which becomes denser upon compression. The missing data points in the raw data for small $q \leq 0.05 \text{ \AA}^{-1}$ are caused by absorber switches. Due to the high scattering contrast, intensity was too high after the absorber switch, thus not properly recorded by the detector.

The scattering length density perpendicular to the interface is described by N equally sized boxes. In each box of size a , the scattering length density is constant. The edge of each box is modulated by an error function with a width σ to smooth the transition between two



Π	number of boxes N	box size a	width σ
10 mN/m	6	1.0 nm	0.4 nm
18 mN/m	6	1.1 nm	0.4 nm
26 mN/m	8	1.4 nm	0.4 nm

Figure 3: X-ray reflectivity data of FeNP5 films measured at three different positions in the isotherm. For comparison the reflectivity of the bare water interface was measured prior to film preparation. The solid lines demonstrate the good agreement between the used box-model (equation 4) and the data. The resulting normalised scattering length density profiles are shown below. The water surface is placed at $z = 0$ and negative values of z correspond to increasing height above the water surface. Important fitting parameters are depicted in the table below.

neighbouring boxes. To keep the model as simple as possible, the lowest number of boxes N resulting in a reasonable description of the data was chosen. Finally, the scattering length density profile of the film is given by

$$\langle \rho(z) \rangle = \sum_{j=1}^N \frac{\Delta \rho_j}{2} \left(1 + \operatorname{erf} \left(\frac{z + j \cdot a}{\sqrt{2}\sigma} \right) \right) + \frac{\rho_{\text{water}} - \sum_{j=1}^N \Delta \rho_j}{2} \left(1 + \operatorname{erf} \left(\frac{z}{\sqrt{2}\sigma_0} \right) \right) \quad (4)$$

with $\Delta \rho_j$ as the increase or decrease of the scattering length density between each box and

z as the distance from the air-water interface ($z < 0$ for air).

Film thickness was measured for three different positions in the isotherm of the FeNP5 film. The raw reflectivity curves are shown in figure 3 compared to the bare water interface. Their positions in the isotherm are highlighted in the inset. In all curves a very good agreement between model and experimental data is found as demonstrated by the full black lines in the figure. Scattering length density profiles normalised by ρ_{water} are shown in the right panel of the figure. The other important parameters of the model (N , a and σ) are summarized in the table below the figure. For a surface pressure of $\Pi = 10 \text{ mN/m}$ (yellow points), a broad minimum can be observed in raw data. A model for a single particle film of 6 nm thickness is able to describe the data. The second measurement was performed at $\Pi = 18 \text{ mN/m}$ (green points) just before the transition in the compression isotherm occurs. The minimum separates into two clear minima and the model for a single particle film still agrees with the experimental data. The thickness slightly increases to 6.6 nm while the scattering length density profile also indicates that the particle film is more compressed. The last measurement was performed at $\Pi = 26 \text{ mN/m}$ right after the transition occurred. The appearance of two additional minima already indicates that the structure of the film changed substantially. A model consisting of 8 boxes provides a very good description of the data for $q_z \leq 0.25 \text{ \AA}^{-1}$. The overall thickness of the layer increases to 11.2 nm. The scattering length density profile also changes its shape. Instead of one single maximum positioned roughly at half the particle size, a second maximum at larger distances from the interface appears. From the shape of the isotherms we already expected multilayer formation when increasing the surface pressure beyond 18 mN/m. This picture is confirmed by the SLD profile measured at 26 mN/m. The overall film thickness almost doubles and the appearance of the second maximum points to the formation of a second layer of nanoparticles on top of the already existing layer. A cartoon-like representation of the arrangement of nanoparticles with increasing pressure is shown in figure 4.

Furthermore, the absolute values of the scattering length density curves allow to cal-

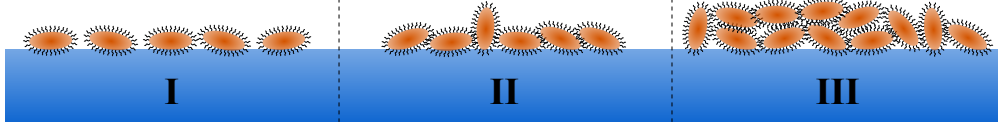


Figure 4: The sketch illustrates the possible different orientations of anisotropic FeNP5 particles at the air-water interface. The three regimes correspond to the three different surface pressures investigated by XRR.

calculate the particle density in the film. For bulk iron oxide, the scattering length density is $\rho_{\text{iron oxide}} = 40.7 \cdot 10^{-6} \text{ \AA}^{-2}$, four times larger than water ($\rho_{\text{water}} = 9.4 \cdot 10^{-6} \text{ \AA}^{-2}$). Since the oleic acid shell does not show any scattering contrast to water, we estimate the scattering length density of the shell to be equal to that of water. Assuming interpenetrating shell ligands, as already discussed above, and a maximum packing density of two dimensional spheres or ellipses of 0.9, the maximum scattering length density of the film can be calculated to $\rho_{\text{SLD}_{\text{min}}} = 2.31 \cdot \rho_{\text{water}}$ and $\rho_{\text{SLD}_{\text{maj}}} = 2.83 \cdot \rho_{\text{water}}$ for standing and flat configuration respectively. From the shape of the isotherm discussed in accordance to figure 2, we would expect a dense packing of the flat configuration right before the shoulder, around the $\Pi = 18 \text{ mN/m}$ measurement. The maximum value of the scattering length density profile in this case is $1.9 \cdot \rho_{\text{water}}$, roughly 70 % of the estimated value. Thus, the particle density in the film has to be reduced accordingly, which means that the mean molecular areas discussed in the previous paragraph seem strongly overestimated (roughly by a factor of three based on the XRR profiles). These interpretations are further supported by observations during film preparation. After spreading the sample solution a substantial staining of the metal parts of the Hamilton syringe is visible, a clear indication of remaining nanoparticles that are missing in the layer.

For the FeNP10 film, reflectivity was also measured for three different positions in the isotherm. Raw data is shown in figure 5 with the measurement position highlighted in the inset of the figure. Interference patterns are visible for all film measurements. The most distinct minima are visible for the highest surface pressure, however, the same features are also visible for the two lower surface pressures. There is no strong shift in the positions. A

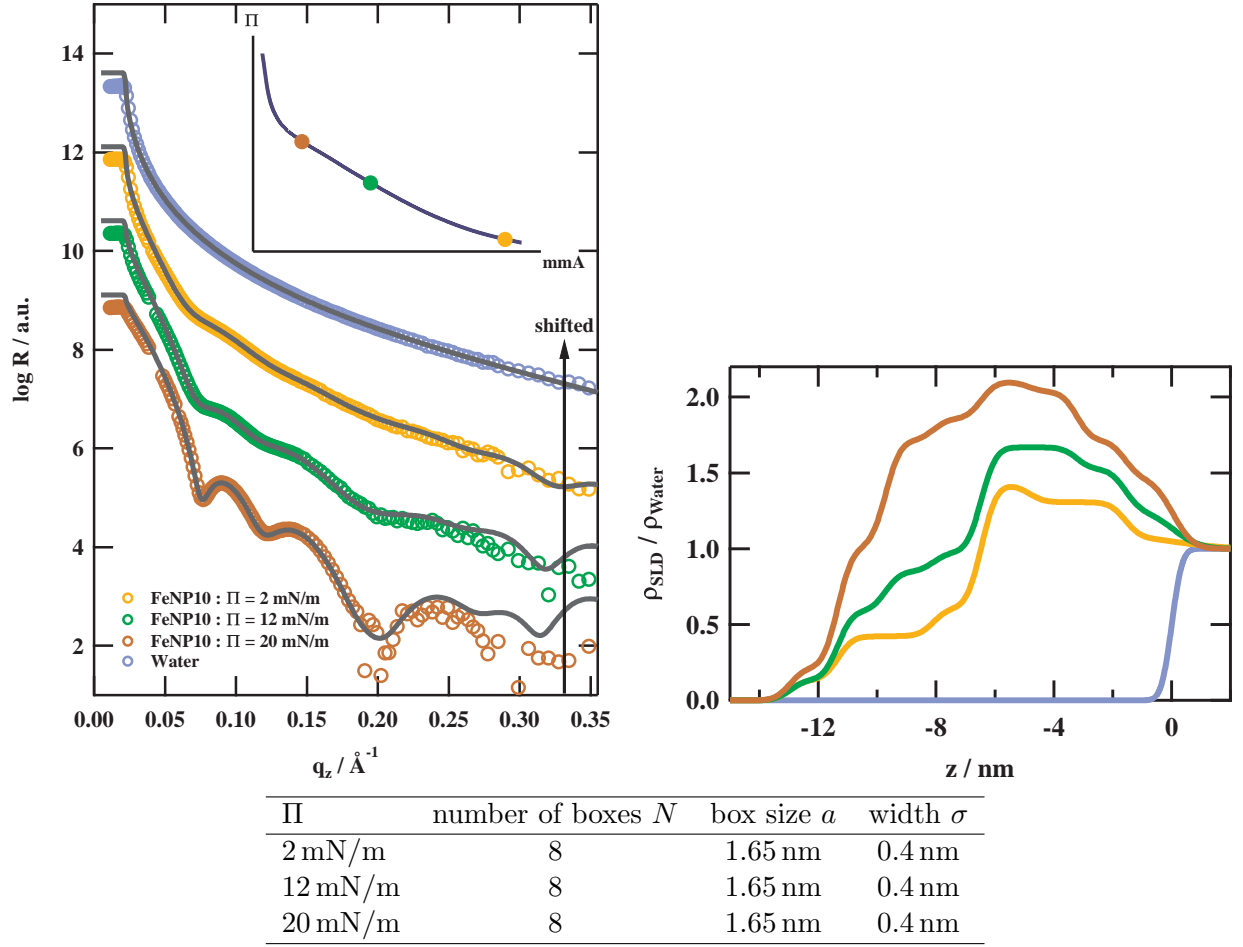


Figure 5: X-ray reflectivity data of FeNP10 films measured at three different positions in the isotherm. For comparison the reflectivity of the bare water interface was measured prior to film preparation. The solid lines demonstrate the good agreement between the used box-model (equation 4) and the data. The resulting normalised scattering length density profiles are shown below. The water surface is placed at $z = 0$ and negative values of z correspond to increasing height above the water surface. Important fitting parameters are depicted in the table below.

very good agreement between model and experimental data is demonstrated by the full lines for $q_z \leq 0.25 \text{ \AA}^{-1}$. The model described by equation (4) is used with 8 boxes, each having a size of 1.65 nm and a σ of 0.4 nm. The overall thickness of 13.2 nm for the layer compares very well with the particle size obtained from the form factor fit of the SAXS data.

The normalized scattering length density profiles at the right panel of figure 5 indicate that particles are moving closer together upon compression. Scattering length density increases but film thickness is the same. We see no indication for multilayer formation which

is consistent with results from Langmuir isotherms.

Analysing the absolute values of the scattering length density, the same overestimation of mmA as discussed for the FeNP5 particles is found. For a densely packed film of FeNP10 particles with interpenetrating shell a maximum scattering length density of $3.0 \cdot \rho_{\text{water}}$ can be estimated. From the shape of the isotherm such a dense packing can be assumed at the highest investigated surface pressure of $\Pi = 20 \text{ mN/m}$. However, we only measure a value of $2.1 \cdot \rho_{\text{water}}$, which is 70 % of the expected value. Again, the mmA seems to be overestimated by a factor of three as already discussed for the smaller particles.

Polymer Nanocomposite Films

The two presented sizes of iron oxide nanoparticles form single particle layers at the air-water interface (at sufficiently low surface pressure) and therefore seem to be promising candidates for the formation of polymer nanocomposite films. In a previous publication, we presented a block copolymer PEG₆-*b*-P*n*BA₁₃₂ that forms very stable films at the air-water interface.²⁶ The polymer spreads as a thin layer (thickness around 2 – 3 nm) and has a very characteristic isotherm. One unique feature is a long constant pressure plateau in the isotherm in which polymer chains dewet from the air-water interface. Furthermore, the 2D radius of gyration for one chain is approximately 60 nm² which is comparable to the size of the FeNP5 and FeNP10 particles (FeNP5: 27 or 70 nm² and FeNP10: 129 nm²).

The two composite solutions were prepared by adding polymer to the iron oxide nanoparticles dissolved in chloroform. SAXS measurements of the form factor (data shown in ESI) demonstrate that addition of polymer does not lead to aggregation of the particles. The same particle form factors are observed as in the toluene solutions of the nanoparticles. The particle concentration for both composites was chosen such as to have a coverage of 3 % of the area in a film prepared at the air-water interface before compression. The composite films were prepared for low surface coverage and compression isotherms were recorded. The

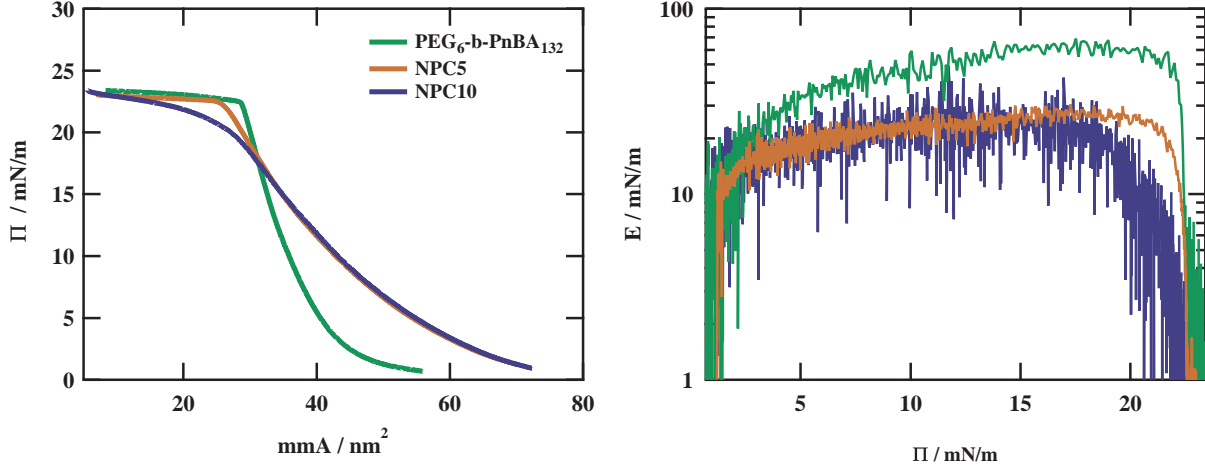


Figure 6: Langmuir isotherms presented as surface pressure (Π) vs. mean molecular area (mmA) for NPC5, NPC10 and the pure polymer film. The elastic modulus (E) computed from the isotherms is depicted below as E vs. Π .

mixture of FeNP5 will be referred to as NPC5, and NPC10 for FeNP10.

Langmuir Isotherms of Composite Layers

We now compare the compression isotherms of the composites with the isotherms of the pure polymer layer. Results of these measurements are shown in figure 6. They are presented as surface pressure Π over the mean molecular area mmA for a polymer chain. For the composites, the area covered by nanoparticles is subtracted from the mmA so that the composite and polymer isotherms can be directly compared. The isotherms of NPC5 and NPC10 are closer to the polymer isotherm than to that of the pure nanoparticles (see figure 2). The surface pressure increases for similar areas indicating that the polymer is predominately responsible for the compression behaviour of the composite. However, in detail the compression behaviour of the three systems is different. For the composite films the surface pressure starts to increase already for larger areas compared to the polymer film. After reaching a critical surface pressure of $\Pi_C \approx 22 - 23 \text{ mN/m}$, a kink can be observed for the pure polymer and NPC5 film at almost the same value of mmA . Further compression of both films does not lead to any increase in surface pressure. In case of the pure polymer system,

the constant pressure plateau has been identified as polymer dewetting the air-water interface.²⁶ The overall similarity between the pure polymer and NPC5 isotherms suggests that this dewetting mechanism is also found in the composite. No signs of buckling and multilayer formation are found in this isotherm. This is presumably due to the significantly reduced density of nanoparticles in the composite film, in comparison to the pure nanoparticle ones.

For NPC10 the similarity to the pure polymer isotherm is not as obvious. Although the low pressure regime of the composite isotherms ($\Pi \leq 15$ mN/m) is almost identical, neither a sharp kink nor a constant pressure plateau can be observed for the NPC10 system. Instead the slope of the NPC10 isotherm starts to flatten out already at a higher mmA but without reaching a plateau at the highest investigated compressions.

The right panel of figure 6 shows the elastic modulus E vs. Π as a representative measure of the resistance of the film upon exhibiting an external force (see equation (3)). In case of the polymer film, a broad plateau can be observed with $E_{\max} \approx 60$ mN/m before asymptotically vanishing for the critical surface pressure Π_C . For NPC5, the shape of E is quite similar. However, absolute values of the modulus are different. In case of the pure FeNP5 film, we measure a lower E modulus (see figure 2) which is caused by the interactions between the oleic acid shell molecules. The E modulus of the composites is reduced by the interaction of shell molecules with surrounding particles and polymers. The fluctuations of E are stronger for the composite compared to the polymer while we observe the same deviation upon reaching Π_C . When comparing NPC10 to NPC5, two disparities become apparent. First of all, the E modulus decreases more slowly for higher surface pressures ($\Pi > 15$ mN/m). The absolute value for E is approximately the same, but the fluctuations become even more pronounced. These fluctuations may indicate the existence of larger structures within the film. Obviously these structures have to be related to the iron oxide nanoparticles and the fluctuations may be related to aggregation of nanoparticles in the polymer matrix. FeNP10 affects the elastic properties of the film more strongly than FeNP5 although the area covered by particles is the same for both composites. To further investigate this behaviour it is therefore important

to obtain information on the distribution of the nanoparticles inside the polymer matrix. To find this distribution we followed two different experimental approaches. The first one was to determine the film thickness and density profile by performing in-situ XRR experiments on the composites spread at the air-water interface. In another experiment, the composites were transferred on silicon wafers using the Langmuir-Blodgett technique and an ex-situ AFM experiment was used to investigate the distribution of particles. Results of the in-situ approach will be discussed first.

Vertical Density Profiles of Composite Layers at the Air-Water Interface

Specular reflectivities were measured in-situ for four positions in the isotherms of both composite films to study film morphology. Results for both nanoparticles and films at different compressions are compiled in figure 7. Due to the high contrast of the iron oxide nanoparticles and the smoothness of the films, interference patterns can be observed in the raw data of both composite films (upper panel of figure 7). Up to a scattering vector of $q_z \leq 0.3 \text{ \AA}^{-1}$ a very good agreement between the raw data and the multilayer model introduced in equation (4) is demonstrated by the full black lines. Six boxes of equal size ($a = 0.9 \text{ nm}$ and $\sigma = 0.3 \text{ nm}$) were used to describe the NPC5 film, while eight were necessary for NPC10 ($a = 1.2 \text{ nm}$ and $\sigma = 0.4 \text{ nm}$). This leads to an overall thickness of 5.6 nm for NPC5 and 9.6 nm for NPC10. This shows that no multilayer is formed for either size of nanoparticles, instead particles are immersed in the polymer layer. The normalized scattering length density profiles in the bottom panel of figure 7 are shown for all investigated positions in the isotherm and compared to that of the pure nanoparticle films (dashed grey lines, measured at $\Pi = 10 \text{ mN/m}$ for FeNP5 and $\Pi = 12 \text{ mN/m}$ for FeNP10).

The maximum scattering length density is almost equal for composites and pure nanoparticle films (intermediate surface pressure). However, the shape of the composite profiles have one common feature that clearly separates them from the pure particle films, which is the

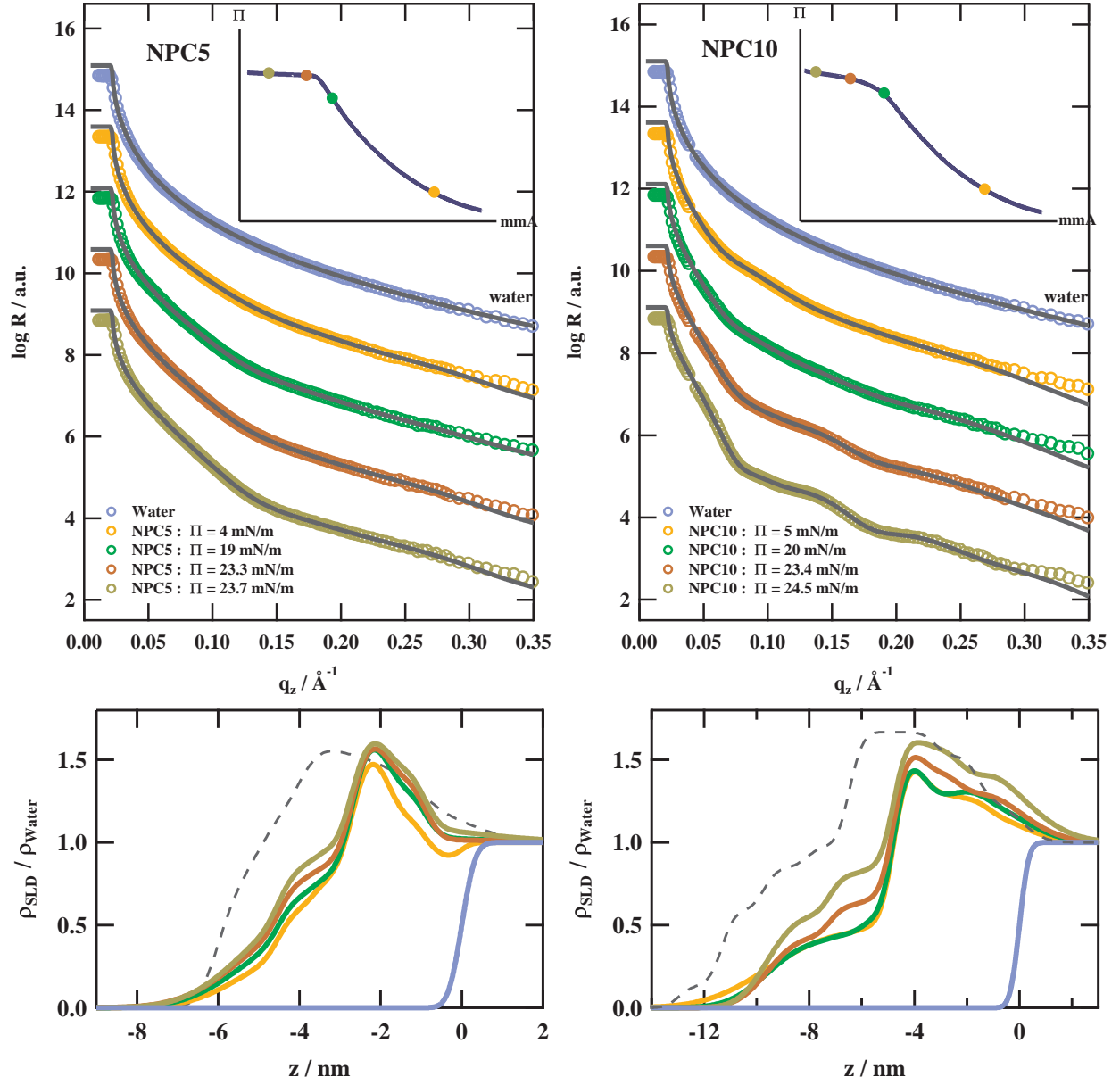


Figure 7: X-ray reflectivity data of NPC5 and NPC10 films both measured at four different positions in the isotherm. For comparison the reflectivity of the bare water interface was measured prior to film preparation. The solid lines demonstrate the good agreement between the used box-model (equation 4) and the data. The resulting normalised scattering length density profiles are shown below. The dashed lines represent the SLD profile at intermediate pressure of the respective pure particle film (details see text).

sharp decrease of the scattering length density for $z \approx -3 \text{ nm}$ (NPC5) respectively $z \approx -4 \text{ nm}$ (NPC10). This feature can be related to the upper limit of the polymer film. The scattering length density of the polymer is similar to water or the shell of the particles. The reflectivity

experiment measures a laterally averaged scattering length density. This average comprises nanoparticles and polymer for small distances from the substrate and nanoparticles and air for distances larger than the polymer film thickness. Therefore, we can identify the polymer film in the density profiles of the composite films with a thickness of 3 nm to 4 nm. This is in good agreement with the thickness of the pure polymer film.²⁶

The in-situ XRR measurements show that nanoparticles are present within the composite films. However, specular reflectivity measures the film thickness as an average over the interface, in contrast to that off-specular scattering gives access to the lateral distribution of the particles inside the film. Off-specular data was also recorded for the films, but it was not possible to separate the scattering of a single particle (form factor) from the contribution of the height-height correlation function (see ESI). Still, the different compression behaviour for the two composites indicates that there must be a structural difference. In order to follow this question further LB films were transferred on silicon wafers at $\Pi = 15 \text{ mN/m}$ to be investigated using AFM. This should provide information on the lateral distribution of nanoparticles in the composite layer.

Lateral Distribution of Nanoparticles in Composite Layers

Results of the AFM measurements are shown in figure 8 for NPC5 (left panel) and NPC10 (right panel). Both images show an area of $22 \mu\text{m} \times 22 \mu\text{m}$ while the maximum height of the observed structures is less than 30 nm. Therefore, particles are essentially confined in 2D. The observed objects are distributed in a continuous matrix, which has to be the polymer film. We thus have a complete coverage of the investigated area on the silicon wafer by the polymer nanocomposite. We note that lateral dimensions are a convolution of cantilever and object size, thus lateral sizes appear significantly larger.³⁸ The insets in the images show higher resolution scans of selected regions on the silicon wafer. Single nanoparticles can be clearly identified as shown in the inset of the figure and there is a very obvious difference between NPC5 and NPC10 films. In case of NPC5, the lateral distribution of FeNP5 in the

polymer matrix is given by many almost disk-like domains (left panel). The high resolution image indicates the presence of single particles as well as small clusters of only few particles. Obviously, the aggregation behaviour of both nanoparticles is very different. For NPC10, we observe chain-like structures of different sizes (right panel). To quantitatively investigate the different aggregation behaviour of NPC5 and NPC10, we analyse these images further. We first identify each connected domain with a height above 4 nm as one single object. For every object the radius of gyration r_g in pixels ($1 \text{ px} \hat{=} 30 \text{ nm}$) is calculated and compared to its area (defined by the number of occupied pixels N). Images from three different positions of the LB film were used to improve statistics. In total 4644 objects for NPC5 and 266 for NPC10 were considered.

In the bottom of figure 8, we present the results from these considerations. There is a power law relation between the number N and r_g ($N \sim r_g^d$) with a fractal dimension d . We identify a single power law for NPC5 for the full range of observed aggregate sizes while there is a crossover between two different exponents for NPC10. From the exponent of the power law we can determine the fractal dimension d of the structures. The upper limit for 2D structures is $d = 2$ (compact object) and $d = 1$ is the lower limit (straight line). We note that both limits are logical boundaries, however the upper one can be seen in the data on NPC5.

The fractal dimension of $d_{\text{NPC5}} = 1.97 \pm 0.01$ confirms our initial description of almost disk-like objects for FeNP5. In case of NPC10, we find two different power laws. For large structures, the fractal dimension is $d_{\text{NPC10,large}} = 1.13 \pm 0.03$ which is close to the limit of a straight line. This agrees with our initial interpretation of chain-like structures of FeNP10. However, it is interesting that we observe a crossover of the power law for small domains ($r_g < 9 \text{ px}$). Small domains tend to be less extended with a fractal dimension of $d_{\text{NPC10,small}} = 1.74 \pm 0.01$.

Particles with dominating magnetic interaction are expected to form chain like structures, with dipole moments aligned parallel along the chain. Although predicted theoret-

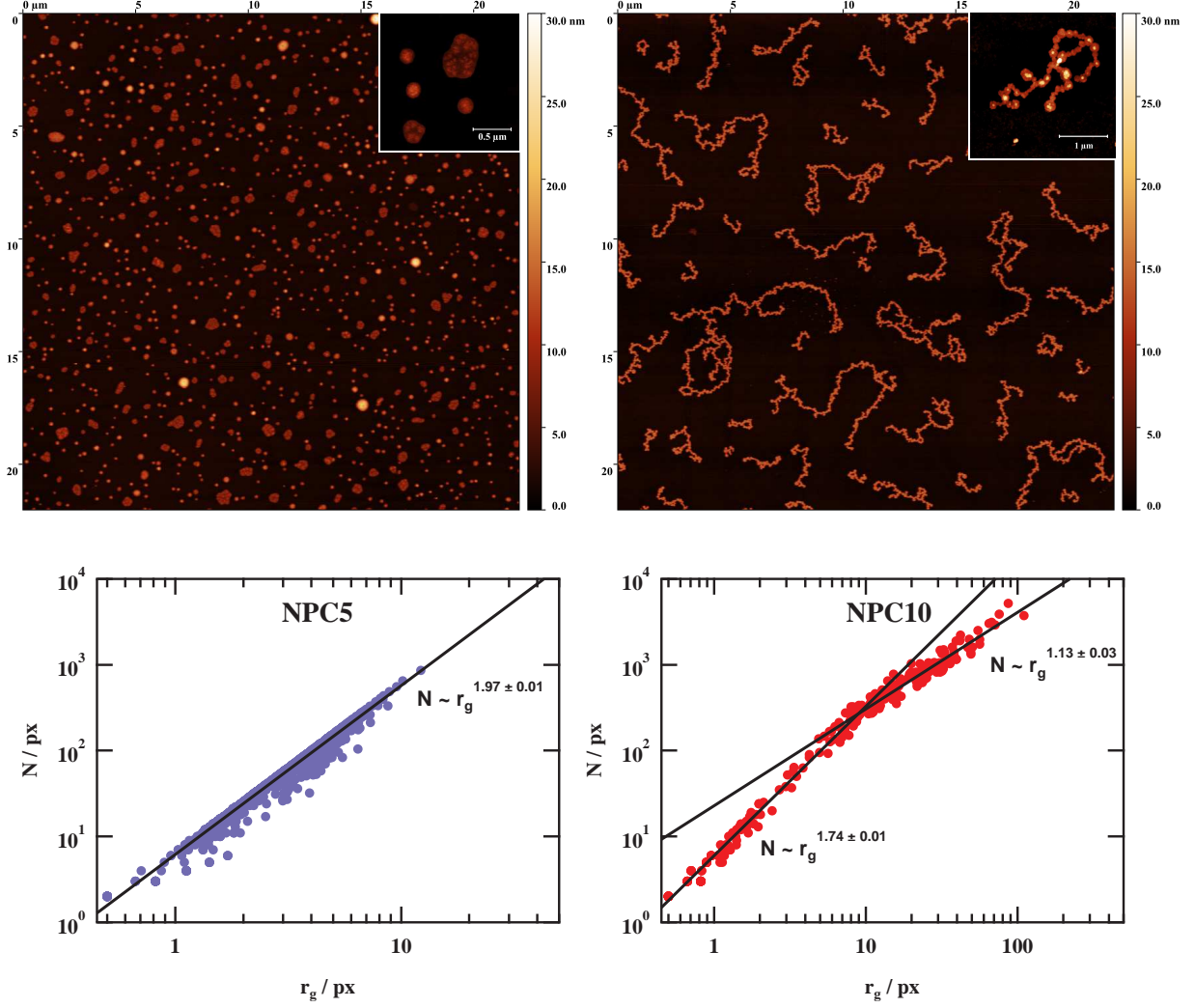


Figure 8: Representative atomic force microscopy images ($22\mu\text{m} \times 22\mu\text{m}$) for NPC5 and NPC10 LB films. High resolution scans of characteristic domains are shown as inset. The bottom panel shows a fractal analysis in which images from three different regions were used for both systems. For every identified object its area (given by the respective number of pixels N) is plotted versus its radius of gyration r_g . The solid lines are power-law fits to the data.

ically and found in many simulations, isolated chains in zero field are rarely observed experimentally.^{27,32,39–42} So far, clear evidence has only been obtained by vitrified cryo-TEM samples.^{21,22} For a dried powder of FeNP10 we can clearly measure a remanent magnetisation $M_R = 0.019 \text{ A nm}^2$ per particle (see ESI). Two-dimensional simulations of aggregating magnetic particles indeed find a fractal dimension of $d = 1.13 \pm 0.01$ for large cluster sizes (several thousand particles).²⁷ This result nicely agrees with our finding for large cluster

sizes even though $k_B T$ should be much larger than the magnetic dipolar interaction energy between two single particles. Here, the presence of the polymer matrix turns out to be the important factor.

A particle approaching a large cluster is driven by Brownian motion, however at the same time it is influenced by the overall magnetic dipole interaction of the cluster. The energetically most favorable position for the particle to attach to the cluster is at either end of the chain. Due to the high viscosity of the polymer, the diffusion coefficient of the particle is low. As a consequence, the trajectory of the particle may be affected more efficiently by the dipolar interaction with the cluster, thus it is more likely moving towards the energetically most favorable position. Although this argument applies to all cluster sizes, we observe a different power law for small clusters. The fractal dimension $d = 1.74 \pm 0.01$ is close to the value for diffusion limited aggregation, DLA ($d = 1.715 \pm 0.004$).^{27,43,44} Particle dynamics in diffusion limited aggregation are fully driven by Brownian motion. Particles do not interact with each other unless they attach. Once attached, they are permanently bound to the cluster. For large cluster sizes, we see a dominating magnetic dipolar interaction between a nanoparticle and already existing clusters. The magnetic dipolar interaction with a small cluster is weak. Therefore, even the reduced diffusion coefficient is not enough to allow for the nanoparticle to be significantly influenced by the magnetic dipolar interaction. 2D Simulation also reproduce this effect.²⁷ Smaller cluster tend to exhibit a fractal dimension close to the DLA case.

Turning to the smaller nanoparticle FeNP5. In measuring the magnetisation curves, we find that FeNP5 has no remanent magnetisation (see ESI), thus it is superparamagnetic. As there is no magnetic driving force, they do not form chain-like aggregates. However, the fractal dimension of FeNP5 clusters is almost two, thus significantly higher as expected for DLA. An explanation can be given by a restructuring process during aggregate formation. After attaching to the cluster, particles are able to slightly move towards the energetically most favorable position. For small clusters this leads to a significant compactification.²⁸

Here, the anisotropy of the particles may be crucial.

The observation on aggregation can also explain the different compression behaviour of the two polymer nanocomposite films. Up to a surface pressure of 15 mN/m the isotherms for both composites are almost identical, thus the compression behaviour seems to be polymer dominated. The LB films investigated by AFM are prepared precisely at this point. For NPC10 the randomly oriented nanoparticle chains can be deformed thus leading to a weaker increase in surface pressure. The compact aggregates in NPC5 can not be further deformed. Their interaction with the polymer matrix is determined by the interaction of the oleic acid molecules and for the investigated concentration of particles compression behaviour is still dominated by the polymer.

Another interesting aspect is the height distribution of the aggregates in the film. We calculated the height distribution by extracting the maximum height for each object in both composites. The same three images per particle size as for the fractal analysis were used. Results for the normalized height distributions are shown in figure 9. For NPC10, a single peak is observed with its maximum at 13.3 nm. This value is in very good agreement with the film thickness measured for the pure FeNP10 films (see figure 5) and the particle size obtained by SAXS (see figure 1). For NPC5, a bimodal distribution is observed with maxima at 8.6 nm and 11.7 nm. Since there is no indication for buckling of the nanoparticle domains in the composite, the two maxima can be related to the spheroidal shape of the FeNP5 and represent flat and flipped configurations. The absence of buckling is not surprising because of the low concentration of nanoparticles in the film and the moderate surface pressure at LB film preparation. In contrast to NPC10 the positions of the maxima are shifted towards larger sizes in comparison to SAXS results. The difference is around 4 nm which is comparable to the thickness of the polymer film. The in-situ XRR results indicate that the nanoparticles are distributed within the polymer film, however different surface affinities towards the silicon wafer may lead to a rearrangement, resulting in nanoparticles being pushed out of the polymer film. Since FeNP5 are smaller than the size of the polymer chain,

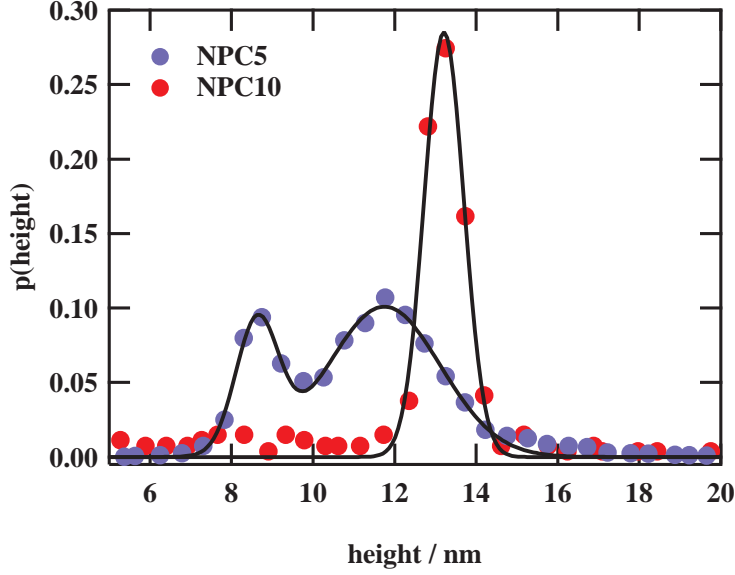


Figure 9: Height distribution of identified objects for NPC5 and NPC10 LB films. For the anisotropic FeNP5 a bimodal distribution is found, while FeNP10 exhibit a single maximum. Full lines represent guides for the eye.

this scenario seems more likely for these particles than for the larger ones.

Conclusion

In this study we investigated the structural properties of iron oxide nanoparticles at the air-water interface. Three different sizes of particles were characterised by small angle X-ray scattering (SAXS). All samples showed a narrow size distribution but only the two larger ones ($d_{\text{FeNP10}} = 12.8 \text{ nm}$, $d_{\text{FeNP20}} = 21.4 \text{ nm}$) are of spherical shape, while the smallest one is an oblate spheroid ($d_{\text{FeNP5}_{\text{min}}} = 3.7 \text{ nm}$, $d_{\text{FeNP5}_{\text{maj}}} = 9.4 \text{ nm}$). While FeNP20 particles do not form stable monolayers at the interface, the film structure and compression behaviour of FeNP5 and FeNP10 can be nicely characterised. At high surface pressures ($\Pi \leq 18 \text{ mN/m}$) FeNP5 particles form a double layer, which may be facilitated by the anisotropic shape of these particles.

FeNP5 and FeNP10 can be introduced in a thin polymer matrix and form stable polymer nanocomposites at the air-water interface. XRR shows that nanoparticles are immersed

in a 3 nm to 4 nm thick polymer layer at the air-water interface. On LB films, the height distribution of aggregates seen by AFM reproduces the particle sizes measured by SAXS and XRR. FeNP5 is superparamagnetic and forms small compact aggregates within transferred structures (LB film). The formation of these aggregates can be explained by diffusion limited aggregation (DLA) in the limit of small cluster sizes with dominating restructuring effects.²⁸ In contrast, FeNP10 is ferromagnetic and therefore forms open, chain-like aggregates due to an alignment of their magnetic moments along the chain. The existence of such randomly oriented chains of magnetic particles has been predicted by de Gennes theoretically even in the absence of an external magnetic field.³⁹ Their existence has also been observed in magnetotactic bacteria as linear chains of magnetic nanoparticles coated with a lipid biomembrane.^{45,46} 2D simulations find a fractal dimension of 1.13 for sufficiently large aggregates for particles with dominating magnetic interaction.^{27,40} Although thermal energy should be dominating in this system, our results nicely agree with these predictions for large cluster sizes. We explain this by the presence of the polymer matrix providing a highly viscous environment for the nanoparticles. Therefore, nanoparticles are more easily guided towards the energetically most favorable position in the cluster. For small cluster sizes the reduced diffusion coefficient of the particles can not compensate the small magnetic field provided by the aggregate. Their fractal dimension is $d = 1.74$, close to the DLA value.

Acknowledgements

The authors gratefully acknowledge Professor Dr. Oliver Gutfleisch and his group for performing the magnetisation measurements.

References

- (1) Kelly, K. L.; Coronado, E.; Zhao, L. L.; Schatz, G. C. The Optical Properties of Metal Nanoparticles: The Influence of Size, Shape, and Dielectric Environment. *The Journal*

- of Physical Chemistry B* **2003**, *107*, 668–677.
- (2) Balazs, A. C.; Emrick, T.; Russell, T. P. Nanoparticle Polymer Composites: Where Two Small Worlds Meet. *Science* **2006**, *314*, 1107–1110.
 - (3) Winey, K. I.; Vaia, R. A. Polymer Nanocomposites. *MRS Bulletin* **2007**, *32*, 314–322.
 - (4) Hanemann, T.; Szabó, D. V. Polymer-Nanoparticle Composites: From Synthesis to Modern Applications. *Materials* **2010**, *3*, 3468–3517.
 - (5) Kumar, S. K.; Benicewicz, B. C.; Vaia, R. A.; Winey, K. I. 50th Anniversary Perspective: Are Polymer Nanocomposites Practical for Applications? *Macromolecules* **2017**, *50*, 714–731.
 - (6) Chevigny, C.; Dalmas, F.; Di Cola, E.; Gigmes, D.; Bertin, D.; Boué, F.; Jestin, J. Polymer-Grafted-Nanoparticles Nanocomposites: Dispersion, Grafted Chain Conformation, and Rheological Behavior. *Macromolecules* **2011**, *44*, 122–133.
 - (7) Chandran, S.; Begam, N.; Basu, J. K. Dispersion of polymer grafted nanoparticles in polymer nanocomposite films: Insights from surface x-ray scattering and microscopy. *Journal of Applied Physics* **2014**, *116*, 222203.
 - (8) Jiang, N.; Endoh, M. K.; Koga, T.; Masui, T.; Kishimoto, H.; Nagao, M.; Satija, S. K.; Taniguchi, T. Nanostructures and Dynamics of Macromolecules Bound to Attractive Filler Surfaces. *ACS Macro Letters* **2015**, *4*, 838–842.
 - (9) Starr, F. W.; Douglas, J. F.; Meng, D.; Kumar, S. K. Bound Layers Cloak Nanoparticles in Strongly Interacting Polymer Nanocomposites. *ACS Nano* **2016**, *10*, 10960–10965, PMID: 28024345.
 - (10) Zhou, J.; Ralston, J.; Sedev, R.; Beattie, D. A. Functionalized gold nanoparticles: Synthesis, structure and colloid stability. *Journal of Colloid and Interface Science* **2009**, *331*, 251 – 262.

- (11) White, R. J.; Luque, R.; Budarin, V. L.; Clark, J. H.; Macquarrie, D. J. Supported metal nanoparticles on porous materials. Methods and applications. *Chem. Soc. Rev.* **2009**, *38*, 481–494.
- (12) Jain, P. K.; Huang, X.; El-Sayed, I. H.; El-Sayed, M. A. Noble Metals on the Nanoscale: Optical and Photothermal Properties and Some Applications in Imaging, Sensing, Biology, and Medicine. *Accounts of Chemical Research* **2008**, *41*, 1578–1586, PMID: 18447366.
- (13) Mayer, K. M.; Hafner, J. H. Localized Surface Plasmon Resonance Sensors. *Chemical Reviews* **2011**, *111*, 3828–3857, PMID: 21648956.
- (14) Leslie-Pelecky, D. L.; Rieke, R. D. Magnetic Properties of Nanostructured Materials. *Chemistry of Materials* **1996**, *8*, 1770–1783.
- (15) Skomski, R. Nanomagnetism. *Journal of Physics: Condensed Matter* **2003**, *15*, R841–R896.
- (16) Gao, J.; Gu, H.; Xu, B. Multifunctional Magnetic Nanoparticles: Design, Synthesis, and Biomedical Applications. *Accounts of Chemical Research* **2009**, *42*, 1097–1107, PMID: 19476332.
- (17) Bedanta, S.; Kleemann, W. Supermagnetism. *Journal of Physics D: Applied Physics* **2008**, *42*, 013001.
- (18) Koplovitz, G.; Leitus, G.; Ghosh, S.; Bloom, B. P.; Yochelis, S.; Rotem, D.; Vischio, F.; Striccoli, M.; Fanizza, E.; Naaman, R.; Waldeck, D. H.; Porath, D.; Paltiel, Y. Single Domain 10 nm Ferromagnetism Imprinted on Superparamagnetic Nanoparticles Using Chiral Molecules. *Small* **2019**, *15*, 1804557.
- (19) Luo, W.; Nagel, S. R.; Rosenbaum, T. F.; Rosensweig, R. E. Dipole interactions with random anisotropy in a frozen ferrofluid. *Phys. Rev. Lett.* **1991**, *67*, 2721–2724.

- (20) Teixeira, P. I. C.; Tavares, J. M.; da Gama, M. M. T. The effect of dipolar forces on the structure and thermodynamics of classical fluids. *Journal of Physics: Condensed Matter* **2000**, *12*, R411–R434.
- (21) Butter, K.; Bomans, P.; Frederik, P.; Vroege, G.; Philipse, A. Direct observation of dipolar chains in iron ferrofluids by cryogenic electron microscopy. *Nature Materials* **2003**, *2*, 88–91.
- (22) Klokkenburg, M.; Dullens, R. P. A.; Kegel, W. K.; Ern , B. H.; Philipse, A. P. Quantitative Real-Space Analysis of Self-Assembled Structures of Magnetic Dipolar Colloids. *Phys. Rev. Lett.* **2006**, *96*, 037203.
- (23) Santoyo Salazar, J.; Perez, L.; de Abril, O.; Truong Phuoc, L.; Ihiwakrim, D.; Vazquez, M.; Greneche, J.-M.; Begin-Colin, S.; Pourroy, G. Magnetic Iron Oxide Nanoparticles in 1040 nm Range: Composition in Terms of Magnetite/Maghemite Ratio and Effect on the Magnetic Properties. *Chemistry of Materials* **2011**, *23*, 1379–1386.
- (24) Carvalho, M.; Henriques, F.; Ferreira, L.; Godinho, M.; Cruz, M. Iron oxide nanoparticles: the Influence of synthesis method and size on composition and magnetic properties. *Journal of Solid State Chemistry* **2013**, *201*, 144 – 152.
- (25) Gabbasov, R.; Polikarpov, M.; Cherepanov, V.; Chuev, M.; Mischenko, I.; Lomov, A.; Wang, A.; Panchenko, V. M ssbauer, magnetization and X-ray diffraction characterization methods for iron oxide nanoparticles. *Journal of Magnetism and Magnetic Materials* **2015**, *380*, 111 – 116.
- (26) Appel, C.; Kraska, M.; R ttiger, C.; Gallei, M.; St hn, B. Crossover from semi-dilute to densely packed thin polymer films at the air-water interface and structure formation at thin film breakup. *Soft Matter* **2018**, *14*, 4750–4761.
- (27) Pastor-Satorras, R.; Rub , J. M. Particle-cluster aggregation with dipolar interactions. *Phys. Rev. E* **1995**, *51*, 5994–6003.

- (28) Vicsek, T. Pattern Formation in Diffusion-Limited Aggregation. *Phys. Rev. Lett.* **1984**, *53*, 2281–2284.
- (29) Nelson, A. Co-refinement of multiple-contrast neutron/X-ray reflectivity data using MOTOFIT. *Journal of Applied Crystallography* **2006**, *39*, 273–276.
- (30) Huang, T. C.; Toraya, H.; Blanton, T. N.; Wu, Y. X-ray powder diffraction analysis of silver behenate, a possible low-angle diffraction standard. *Journal of Applied Crystallography* **1993**, *26*, 180–184.
- (31) Nečas, D.; Klapetek, P. Gwyddion: An open-source software for SPM data analysis. *Central European Journal of Physics* **2012**, *10*, 181–188.
- (32) Vorobiev, A.; Khassanov, A.; Ukleev, V.; Snigireva, I.; Konovalov, O. Substantial Difference in Ordering of 10, 15, and 20 nm Iron Oxide Nanoparticles on a Water Surface: In Situ Characterization by the Grazing Incidence X-ray Scattering. *Langmuir* **2015**, *31*, 11639–11648, PMID: 26399881.
- (33) Basavaraj, M. G.; Fuller, G. G.; Fransaer, J.; Vermant, J. Packing, Flipping, and Buckling Transitions in Compressed Monolayers of Ellipsoidal Latex Particles. *Langmuir* **2006**, *22*, 6605–6612, PMID: 16831003.
- (34) Choudhary, K.; Manjuladevi, V.; Gupta, R. K.; Bhattacharyya, P.; Hazra, A.; Kumar, S. Ultrathin Films of TiO₂ Nanoparticles at Interfaces. *Langmuir* **2015**, *31*, 1385–1392, PMID: 25557246.
- (35) Vegso, K.; Siffalovic, P.; Majkova, E.; Jergel, M.; Benkovicova, M.; Kocsis, T.; Weis, M.; Luby, S.; Nygård, K.; Konovalov, O. Nonequilibrium Phases of Nanoparticle Langmuir Films. *Langmuir* **2012**, *28*, 10409–10414, PMID: 22724517.
- (36) You, S. S.; Rashkov, R.; Kanjanaboos, P.; Calderon, I.; Meron, M.; Jaeger, H. M.; Lin, B. Comparison of the Mechanical Properties of Self-Assembled Langmuir Mono-

- layers of Nanoparticles and Phospholipids. *Langmuir* **2013**, *29*, 11751–11757, PMID: 23957531.
- (37) Baba, T.; Takai, K.; Takagi, T.; Kanamori, T. Effect of perfluoroalkyl chain length on monolayer behavior of partially fluorinated oleic acid molecules at the airwater interface. *Chemistry and Physics of Lipids* **2013**, *172-173*, 31 – 39.
- (38) Sievers, S.; Braun, K.-F.; Eberbeck, D.; Gustafsson, S.; Olsson, E.; Schumacher, H. W.; Siegner, U. Quantitative Measurement of the Magnetic Moment of Individual Magnetic Nanoparticles by Magnetic Force Microscopy. *Small* **2012**, *8*, 2675–2679.
- (39) de Gennes, P. G.; Pincus, P. A. Pair correlations in a ferromagnetic colloid. *Physik der kondensierten Materie* **1970**, *11*, 189–198.
- (40) Holm, C.; Weis, J.-J. The structure of ferrofluids: A status report. *Current Opinion in Colloid & Interface Science* **2005**, *10*, 133 – 140.
- (41) Prokopieva, T. A.; Danilov, V. A.; Kantorovich, S. S.; Holm, C. Ground state structures in ferrofluid monolayers. *Phys. Rev. E* **2009**, *80*, 031404.
- (42) Lefebure, S.; Mnager, C.; Cabuil, V.; Assenheimer, M.; Gallet, F.; Flament, C. Langmuir Monolayers of Monodispersed Magnetic Nanoparticles Coated with a Surfactant. *The Journal of Physical Chemistry B* **1998**, *102*, 2733–2738.
- (43) Witten, T. A.; Sander, L. M. Diffusion-limited aggregation. *Phys. Rev. B* **1983**, *27*, 5686–5697.
- (44) Tolman, S.; Meakin, P. Off-lattice and hypercubic-lattice models for diffusion-limited aggregation in dimensionalities 2-8. *Phys. Rev. A* **1989**, *40*, 428–437.
- (45) Ghaisari, S.; Winklhofer, M.; Strauch, P.; Klumpp, S.; Faivre, D. Magnetosome Organization in Magnetotactic Bacteria Unraveled by Ferromagnetic Resonance Spectroscopy. *Biophysical Journal* **2017**, *113*, 637–644.

- (46) Scheffel, A.; Gruska, M.; Faivre, D.; Linaroudis, A.; Plitzko, J. M.; Schüler, D. An acidic protein aligns magnetosomes along a filamentous structure in magnetotactic bacteria. *Nature* **2005**, *440*, 110–114.

Electronic Supporting Information (ESI)

Zero Field Assembly of Long Magnetic Dipolar Chains in 2D Polymer Nanocomposite Films

Christian Appel,^{*,†} Björn Kuttich,[†] Lukas Stühn,[‡] Robert W. Stark,[‡] and Bernd
Stühn[†]

[†]*Institute of Condensed Matter Physics, Technische Universität Darmstadt,
Hochschulstr. 8, D-64289 Darmstadt, Germany*

[‡]*Physics of Surfaces, Technische Universität Darmstadt, Alarich-Weiss-Str. 16,
D-64287 Darmstadt, Germany*

E-mail: christian.appel@fkp.physik.tu-darmstadt.de

Form Factors for SAXS Measurements

For FeNP10 and FeNP20, we used a sphere form factor with a radius r_c and scattering length density difference between particle and solvent $\Delta\rho_{cs}$:

$$F_{\text{sphere}}(q, r_c) = r_c^3 \Delta\rho_{cs} \frac{\sin(qr_c) - qr_c \cos(qr_c)}{(qr_c)^3} \quad (1)$$

Polydispersity (PDI) of the radius is taken into account by a Schulz-Zimm distribution:

$$f(r, r_c) = \frac{1}{PDI^2} \left(\frac{r}{r_c} \right)^{\frac{1}{PDI^2} - 1} \frac{e^{-\frac{r}{PDI^2 r_c}}}{r_c \Gamma\left(\frac{1}{PDI^2}\right)} \quad (2)$$

Scattered intensity can be written as:

$$I(q) \propto \int_0^\infty |F_{\text{sphere}}(q, r)|^2 \cdot f(r, r_c) dr \quad (3)$$

In case of FeNP5, a model for an oblate spheroid was used with minor radius r_{minor} , major radius r_{major} , scattering length density difference $\Delta\rho_{cs}$ and the first order Bessel function $J_1(x)$:

$$F(q) = 4\pi \Delta\rho_{cs} r_{\text{minor}} r_{\text{major}}^2 \frac{J_1(qu)}{qu} \quad (4)$$

$$u = \sqrt{r_{\text{major}}^2 (1 - \alpha^2) + r_{\text{minor}}^2 \alpha^2} \quad (5)$$

The orientation α of the oblate spheroid in respect to the scattering axis is limited by $0 \leq \alpha \leq 1$. Scattered intensity is given by an average over all possible orientation:

$$I(q) \propto \int_0^1 |F(q, u, \alpha)|^2 d\alpha \quad (6)$$

As a consequence, it is not possible to determine polydispersity of the two radii.

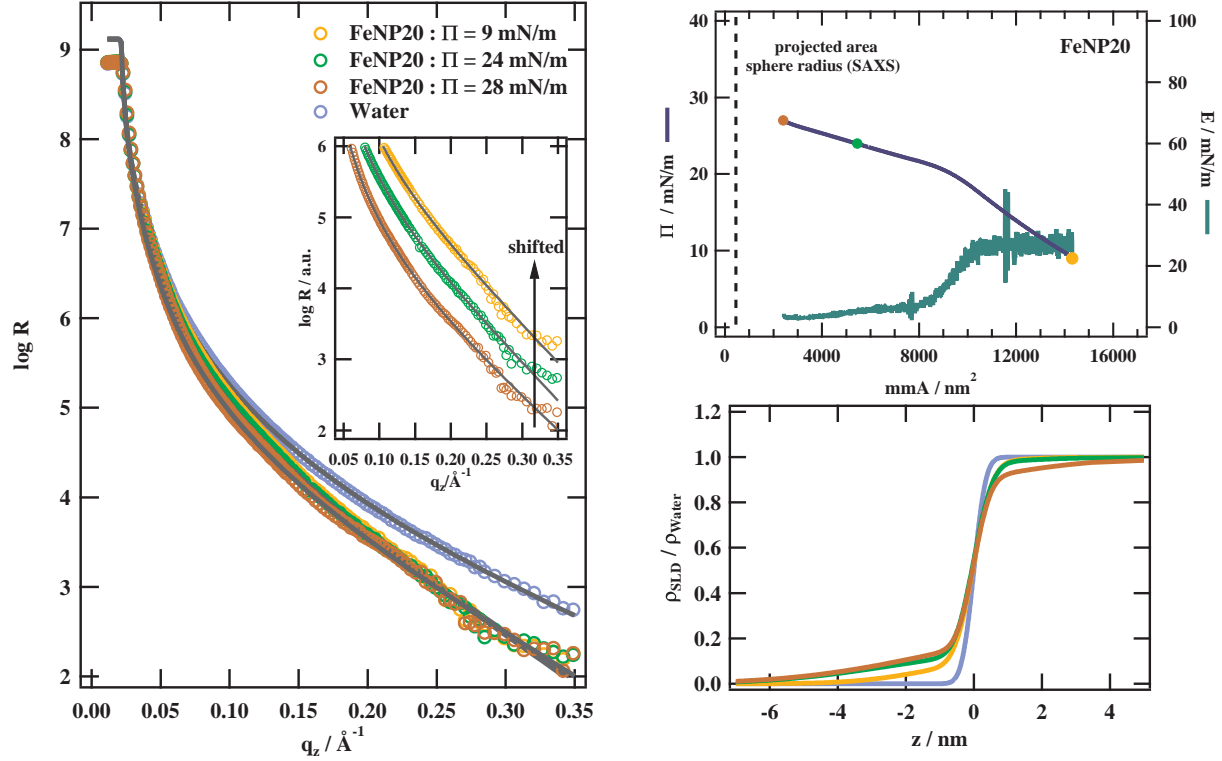


Figure 1: X-Ray reflectivity curves (left hand side) measured for three different positions in the Langmuir isotherm (top panel right hand side) and the bare water surface prior to preparation of the FeNP20 film are shown. The Elastic modulus E computed from the isotherm is depicted too. The bottom panel on the right hand side shows the normalised scattering length density profiles obtained from a one-layer model fitted to the raw data represented by the full lines in the reflectivity curves.

XRR and Langmuir Isotherms of FeNP20 Films

FeNP20 films were prepared at the air-water interface. The surface pressure is already significantly increased ($\Pi \approx 10$ mN/m) for mean molecular areas thirty times larger than the projected particle area measured by SAXS (see Langmuir isotherm in the top panel on the right hand side of figure 1). Reflectivity curves were measured for three different positions in the isotherm as highlighted in the isotherm. The raw data shows essentially a rough surface (see left hand side of figure 1). It can be fitted by a single layer of 2 nm with a roughness around 3 nm. The corresponding normalised scattering length density profiles are shown in the bottom panel on the right hand side of figure 1. There is no evidence for the formation of a single particle film for FeNP20.

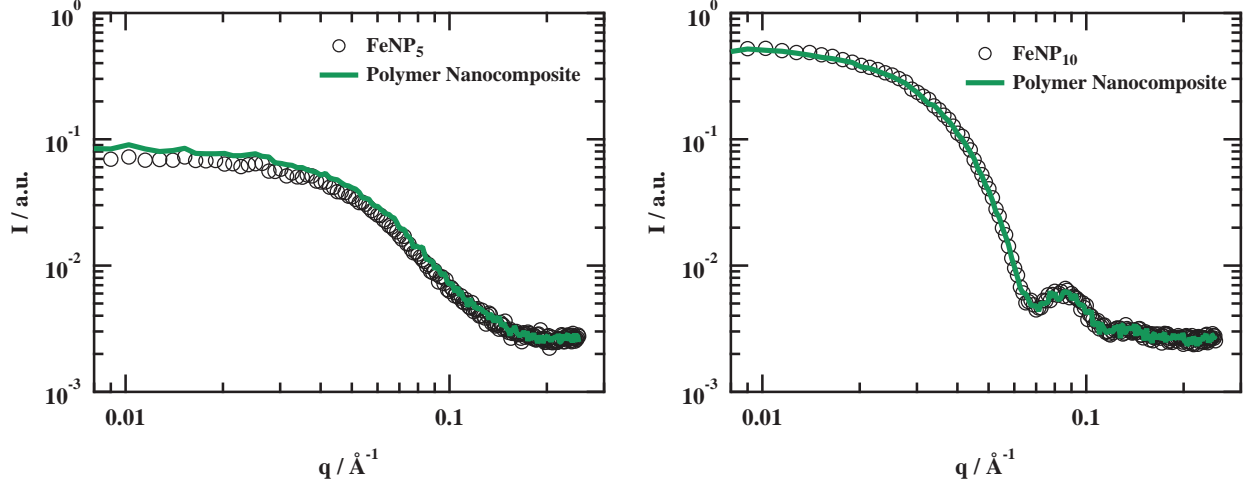


Figure 2: Small angle scattering data from polymer nanocomposites NPC5 (left hand side) and NPC10 (right hand side) dissolved in toluene. Pure particle solutions as shown in the main article are depicted for comparison. There is almost no difference between the curves, thus no evidence of aggregation can be found.

Polymer Nanocomposite Solutions in SAXS

Polymer nanocomposite solutions were prepared as described in the experimental section of the main article. Mixtures of nanoparticles and polymer dissolved in toluene were measured by SAXS. As can be clearly seen in figure 2, obtained data is almost identical to pure nanoparticle solutions. Thus, we conclude that prior to spreading no aggregation is present in the mixtures.

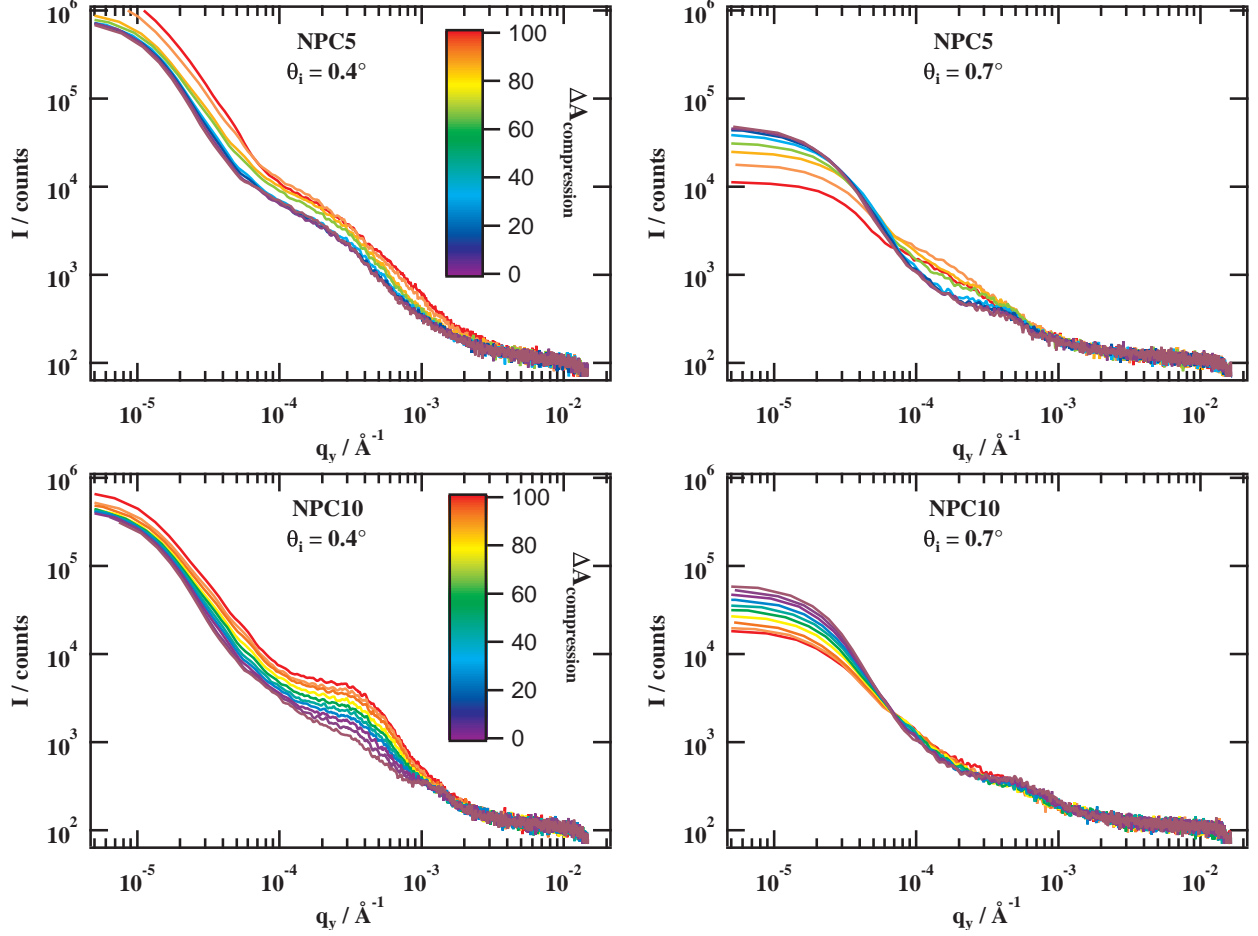


Figure 3: Off-specular intensity for NPC5 (top images) and NPC10 (bottom images) films vs. the in-plane scattering vector q_y . The incident angles are highlighted in the images. The colours refer to consecutive measuring points in the isotherm.

Off-specular Scattering for Polymer Nanocomposites

Off-specular intensity was recorded for NPC5 and NPC10 films for subsequent measurement positions in the isotherm. Figure 3 shows the double logarithmic representation of intensity vs in-plane scattering vector $q_y = 2\pi/\lambda \cdot (\cos(\theta_i) - \cos(\theta_f))$ for NPC5 & NPC10 at two different incident angles θ_i of the X-ray tube. The colour scale represents the percentage of compression after the films were prepared at $\Pi \approx 18 \text{ mN/m}$. Scattering from lateral structures at the interface leads to a signal at a certain q_y , independent of the incident angle θ_i . On the other hand, scattering from bulk structures (such as the form factor of the particles) leads to a signal at a certain $\theta_i + \theta_f$, thus is not fixed to a certain q_y when the

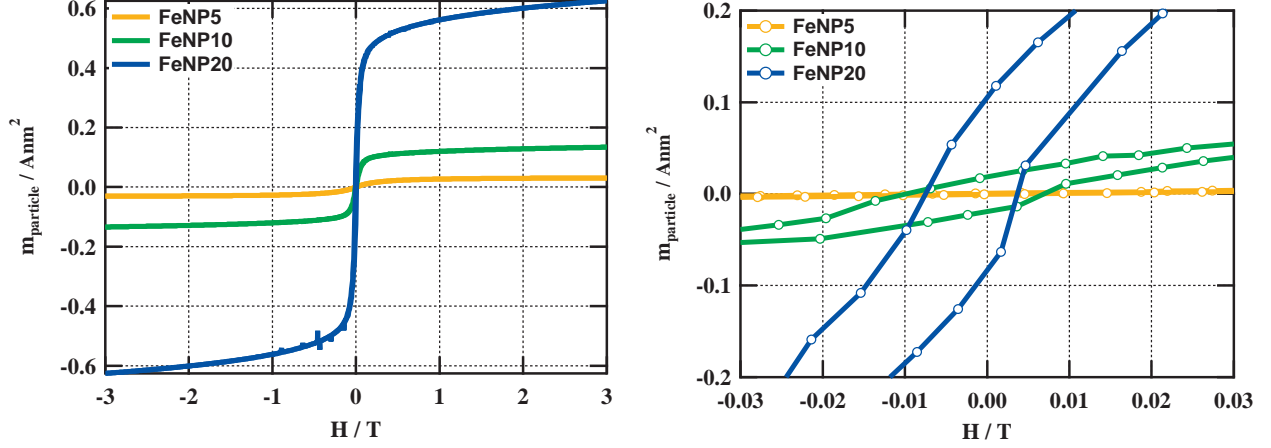


Figure 4: Magnetic hysteresis loops for all particle sizes with full curves shown in the left panel and zoomed around the center in the right panel.

incident angle is changed. Both contributions are measured at the same time and can not be clearly separated. This is shown in the comparison of left and right panel in figure 3. Thus, it is impossible to investigate the surface scattering from the film by in-situ off-specular intensities. The small peak visible for $\theta_i = 0.7^\circ$ at $q_y \approx 5 \cdot 10^{-3}$ (right panel in figure 3) is a scattering artifact of the experiment. It is visible in all spectra for $\theta_i + \theta_f \approx 1.8^\circ$ moving to smaller q_y with increasing θ_i .

Magnetisation curves

Isothermal magnetisation measurements were performed at room temperature using PPMS (Physical Properties Measurement System - Quantum Design PPMS-14) with VSM option (Vibrating Sample Magnetometer), under applied magnetic field up to 3 T. For this, the nanoparticle solutions were dried in a powder sample holder and fixed into a brass half tube holder (Quantum Design).

The left panel of figure 4 shows full magnetic hysteresis loops for all particle sizes. Zoomed curves around the center are shown in the right panel of the figure. It can clearly be seen that the remanent magnetisation vanishes with decreasing particle size. We obtain $M_R = 0.094 \text{ A nm}^2$ for FeNP20 and $M_R = 0.019 \text{ A nm}^2$ for FeNP10.